

# Frequency-dependent rupture process, stress change, and seismogenic mechanism of the 25 April 2015 Nepal Gorkha $M_w$ 7.8 earthquake

YIN JiuXun<sup>1,2</sup>, YAO HuaJian<sup>1,3\*</sup>, YANG HongFeng<sup>2†</sup>, LIU Jing<sup>4</sup>,  
QIN WeiZe<sup>1</sup> & ZHANG HaiJiang<sup>1</sup>

<sup>1</sup>Laboratory of Seismology and Physics of Earth's Interior & School of Earth and Space Sciences, University of Science and Technology of China, Hefei 230026, China;

<sup>2</sup>Earth System Science Programme, Faculty of Science, Chinese University of Hong Kong, Shatin, NT, Hong Kong 999077, China;

<sup>3</sup>National Geophysical Observatory at Mengcheng, University of Science and Technology of China, Mengcheng 233500, China;

<sup>4</sup>State Key Laboratory of Earthquake Dynamics, Institute of Geology, China Earthquake Administration, Beijing 100029, China

Received December 20, 2016; accepted January 31, 2017; published online March 16, 2017

**Abstract** On 25 April 2015, an  $M_w$  7.8 earthquake occurred on the Main Himalaya Thrust fault with a dip angle of  $\sim 7^\circ$  about 77 km northwest of Kathmandu, Nepal. This Nepal Gorkha event is the largest one on the Himalayan thrust belt since 1950. Here we use the compressive sensing method in the frequency domain to track the seismic radiation and rupture process of this event using teleseismic P waves recorded by array stations in North America. We also compute the distribution of static shear stress changes on the fault plane from a coseismic slip model. Our results indicate a dominant east-southeastward unilateral rupture process from the epicenter with an average rupture speed of  $\sim 3$  km  $s^{-1}$ . Coseismic radiation of this earthquake shows clear frequency-dependent features. The lower frequency (0.05–0.3 Hz) radiation mainly originates from large coseismic slip regions with negative coseismic shear stress changes. In comparison, higher frequency (0.3–0.6 Hz) radiation appears to be from the down-dip part around the margin of large slip areas, which has been loaded and presents positive coseismic shear stress changes. We propose an asperity model to interpret this Nepal earthquake sequence and compare the frequency-dependent coseismic radiation with that in subduction zones. Such frequency-dependent radiation indicates the depth-varying frictional properties on the plate interface of the Nepal section in the main Himalaya thrust system, similar to previous findings in oceanic subduction zones. Our findings provide further evidence of the spatial correlation between changes of static stress status on the fault plane and the observed frequency-dependent coseismic radiation during large earthquakes. Our results show that the frequency-dependent coseismic radiation is not only found for megathrust earthquakes in the oceanic subduction environment, but also holds true for thrust events in the continental collision zone.

**Keywords** Nepal Gorkha earthquake, Rupture process, Frequency-dependent seismic radiation, Static shear stress change, Depth varying friction

**Citation:** Yin J X, Yao H J, Yang H F, Liu J, Qin W Z, Zhang H J. 2017. Frequency-dependent rupture process, stress change, and seismogenic mechanism of the 25 April 2015 Nepal Gorkha  $M_w$  7.8 earthquake. *Science China Earth Sciences*, 60, doi: 10.1007/s11430-016-9006-0

## 1. Introduction

On April 25, 2015, an  $M_w$  7.8 earthquake struck Nepal, whose

epicenter located  $\sim 77$  km northwest of Nepal capital, Kathmandu. This earthquake is the largest earthquake since the 1950  $M$ ~8.4 Assam earthquake along the entire Himalayan orogenic belt. In Nepal, the last biggest earthquake is the 1934 Nepal-Bihar  $M_w$  8.1 earthquake (Figure 1). There are 3 large aftershocks ( $M_w$  6.7, 6.8 and 7.3) until May 12, 2015.

\* Corresponding author (email: [hjyao@ustc.edu.cn](mailto:hjyao@ustc.edu.cn))

† Corresponding author (email: [hyang@cuhk.edu.hk](mailto:hyang@cuhk.edu.hk))

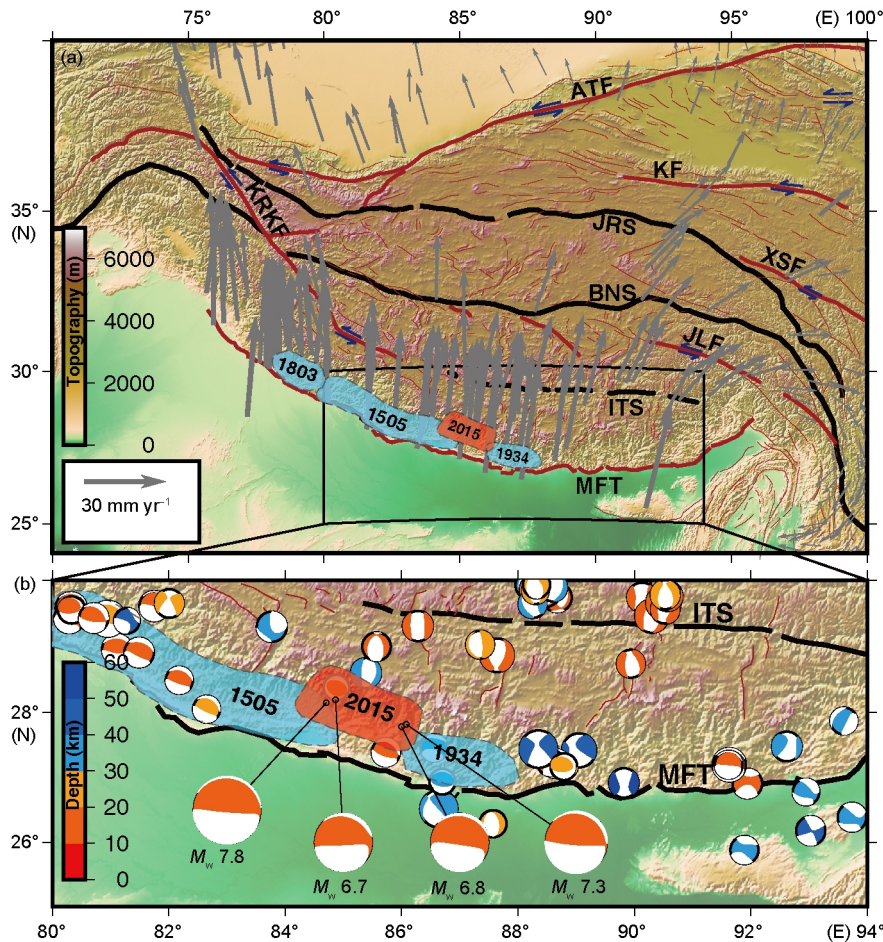


**Figure 1** (a) GPS velocity field showing the surface motion of the Tibetan Plateau relative to the stable Eurasia, as a result of India-Eurasian collision (data from Zhang et al., 2004). Several major active faults are shown as thick red lines: Main Frontal Thrust (MFT), Jiali Fault (JLF), Karakorum Fault (KRKF), Xianshuihe Fault (XSF), Kunlun Fault (KF) and Altyn Tagh Fault (ATF). Bold black lines indicate some major sutures: Indus-Tsangpo Suture (ITS), Bangong-Nujiang Suture (BNS), Jinsha-River Suture (JRS). Thin red lines show small faults in the Tibetan Plateau. Polygons with color fillings indicate estimated rupture extents of some historic large earthquakes in the central Himalayan arc (from Bilham and Ambraseys, 2005). (b) Seismotectonic map near the 2015  $M_w$  7.8 Nepal Gorkha earthquake region. Beach balls (color for focal depths) show mechanisms of historical events as well as the  $M_w$  7.8 Nepal event and three largest aftershocks. Data is from the GCMT catalog (<http://www.globalcmt.org/>). The blue shaded regions show the projected rupture areas for the 1505  $M_w$  8.2 event and 1934  $M_w$  8.1 event (Bilham and Ambraseys, 2005). Approximate rupture region of the 2015 Nepal earthquake series is shown as the red-filling polygon.

The mainshock and the strong aftershocks have killed approximate 9000 people and caused severe property losses to Nepal and its neighboring countries. The 2015 earthquake shows a low-angle north-dipping thrust mechanism as determined by various agencies. Finite fault slip inversions reveal nearly WNW-ESE unilateral rupture characteristics, with a peak slip of 5–7 m (Avoûac et al., 2015; Galetzka et al., 2015; Grandin et al., 2015; Lindsey et al., 2015; Wang and Fialko, 2015; Yue et al., 2016). The overall rupture area of the mainshock spans ~140 km in length and ~70 km in downdip width on the fault interface, but there is no obvious surface rupture, consistent with all published slip inversion models.

Except for the finite fault slip inversion method, the widely used backprojection method is also applied to study the coseismic radiation process during this large earthquake. Backprojection method is first applied to study the 2004 Sumatra  $M_w$  9.2 earthquake, which has extremely long duration

and large rupture area (Ishii et al., 2005). Various groups present their backprojection results of the 2015 Nepal mainshock (Avoûac et al., 2015; Fan and Shearer, 2015; Grandin et al., 2015; Yagi and Okuwaki, 2015; Zhang et al., 2016; Meng et al., 2016; Qin and Yao, 2017). Most of these studies focus on the high-frequency backprojection (e.g. >0.5 Hz) and present a similar pattern in which most of the high-frequency coseismic radiations are originated from the downdip boundary of large slip areas. Recently, these coseismic radiation results are combined with the coseismic slip inversion results (using low-frequency waveform data) and yield more detailed understanding of this earthquake such as multistage rupture processes (Fan and Shearer, 2015) and heterogeneous stress and structural distribution along the rupture propagation direction (Qin and Yao, 2017).

To better understand the rupture process of this event, we investigate frequency-dependent seismic radiation of the

mainshock using the compressive sensing (CS) method (Yao et al., 2011, 2013; Yin and Yao, 2016). The frequency-dependent properties of coseismic radiation have been observed for a few subduction zone megathrust earthquakes (Wang and Mori, 2011; Yao et al., 2011, 2013; Lay et al., 2012; Sufri et al., 2012; Yin et al., 2016). Such frequency-dependent radiation has been attributed to systematic variations of megathrust properties at depth (Lay et al., 2012; Lay, 2015; Ye et al., 2016). More recently, such frequency-dependent radiation has been linked with coseismic shear stress changes during the 2015  $M_w$  8.3 Illapel, Chile earthquake, in which the low-frequency radiation correlates well with the stress-decreasing (releasing) regions while high-frequency radiation sources are mainly within the stress-increasing (loading) regions (Yin et al., 2016). These studies greatly improve our understanding of the rupture process of great earthquakes in subduction zones.

However, it is not well understood whether such depth-varying frictional properties on seismogenic faults hold true in continental regions. Uchide et al. (2013) find that the high-frequency radiation of the 2010 El Mayor-Cucapah, Mexico earthquake is adjacent to the high slip patches, but the low-frequency radiation has not been discussed due to the limitation in spatial resolution of the time-domain backprojection method. The 2015 Nepal event provides us an opportunity to investigate the depth-varying/frequency-dependent rupture processes of large earthquakes in the continental collision environment and to further understand the physics of coseismic radiation within different frequency bands.

In this study, we locate coseismic radiation sources of the 2015 Nepal earthquake in different frequency bands using the CS method. In addition, we compute the shear-stress changes on the fault plane using the slip model from Avouac et al. (2015). We compare our coseismic radiation distribution with the coseismic slip model from finite fault inversion (Avouac et al., 2015), the shear-stress changes (negative static stress drop distribution), and the distribution of available energy calculated from the slip model. Combining these systematic comparisons with previous geophysical studies in this region, we discuss the correlation between frequency-dependent coseismic radiation and the frictional properties of the subducted Indian plate beneath the Himalayas. In the end we discuss seismotectonics in this region and propose one possible seismogenic mechanism of this earthquake.

## 2. Tectonic settings

The source region of the 2015 Nepal earthquake locates in the central Himalayan thrust belt under a strong convergent environment where the Indian plate collides with and plunges beneath the Eurasian plate with a convergence rate of 36–44 mm/yr in the N20°E direction relative to the stable Eurasian plate (e.g. DeMets et al., 1994; Yin and Harrison, 2000;

Molnar and Stock, 2009). Nearly 50% of the convergence ( $\sim 20$  mm yr<sup>-1</sup>) is absorbed at the southern edge of the Tibetan Plateau (Bilham et al., 1997; Larson et al., 1999; Zhang et al., 2004; Bettinelli et al., 2006), leading to accumulated slip of 2 m per century on average in the Himalayas. Most of the slip accumulates as elastic strain on the plate interface of the Main Himalayan Thrust (MHT) in the upper-to-middle crust, which was then periodically ( $\sim 500$  years) released by many large devastating earthquakes along the Himalayas (Bilham and Ambraseys, 2005; Feldl and Bilham, 2006).

The Himalayan thrust belt is manifested by complex multi-fault interaction, steep topographic gradient, and high stress accumulation (Bollinger et al., 2004) due to the plate locking beneath the lesser Himalaya (Ader et al., 2012). It is not rare for large earthquakes to occur in such stress environment, especially for thrust earthquakes (Figure 1). According to the distribution of historical great earthquakes in this region (Bilham et al., 2001; Bilham and Ambraseys, 2005; Feldl and Bilham, 2006), the 2015 mainshock locates between the rupture areas of the 1505  $M_w$  8.2 event and the 1934  $M_w$  8.1 event (Figure 1b), a seismic gap with high shear stress accumulation rate (Ader et al., 2012) since the 1833  $M_w$  7.7 earthquake (Grandin et al., 2015; Bollinger et al., 2016). The 1934 great earthquake ( $M_w$  8.1) only ruptured the southeastern end of the rupture area of the 2015 event (Bollinger et al., 2016). Bilham et al. (2001) have estimated the potential slip along the south edge of the plateau and point out high seismic risk around the 2015 mainshock region.

## 3. Data and methods

### 3.1 Waveform data

In this study, we choose teleseismic P wave data of the 2015  $M_w$  7.8 earthquake from seismic array stations located in Alaska and Northwestern Canada (Figure 2a and b). All data are collected from the Data Management Center of Incorporated Research Institutions for Seismology (IRIS). Since the high frequency contents are relatively weak compared with the low frequency contents (Figure 2c), we first align the waveforms in two frequency bands of 0.05–2 Hz and 0.2–4 Hz, respectively, using the first 8 seconds of the P waves by the waveform cross-correlation method described in Yao et al. (2011). Such alignment can help suppress effects of 3-D structural heterogeneity on travel times along ray paths. Then the aligned waveforms in the 0.05–2 Hz and 0.2–4 Hz frequency bands (Figure 3a and b) are used to invert for source distribution of coseismic radiation within the 0.05–0.3 Hz (LF) and 0.3–0.6 Hz (HF) frequency bands, respectively, using a sliding window scheme (Yao et al., 2011; Yin and Yao, 2016). To better capture the waveform information, we choose the time window length to be 14 s and 6 s for the LF and HF CS results, respectively. The sliding time step is set

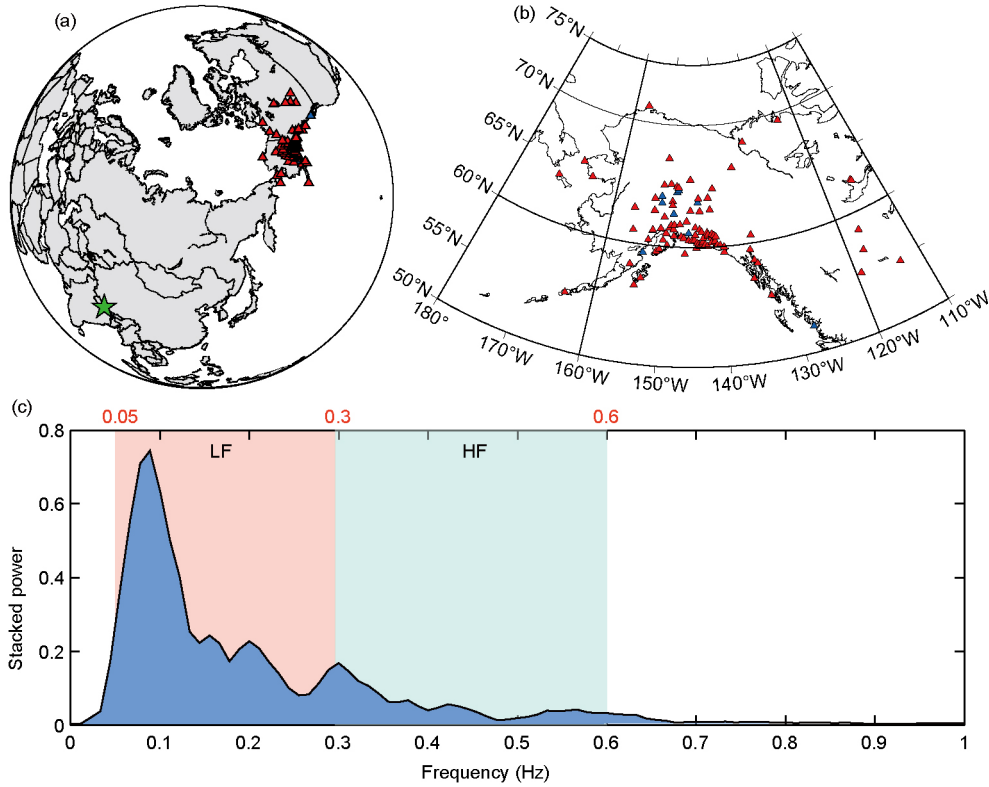


**Figure 2** (a) Map showing locations of the 2015 Nepal event epicenter (green star) and seismic stations in North America (red triangles: stations used for high-frequency results; blue triangles: extra stations used for low frequency results). (b) Enlarged map showing the distribution of the stations in (a). (c) The normalized stacked spectral power of the teleseismic waveforms recorded by the stations in (a) and (b). Background shading highlights the corresponding frequency ranges of low frequency (LF) and high frequency (HF) defined in this study.

to be 2 s. More details of data preprocessing are similar to those in our previous studies (Yin and Yao, 2016).

### 3.2 CS methodology

We apply the CS method to locate sparse seismic radiation sources during earthquake rupture. The CS method is first developed from the signal processing and applied mathematics community (e.g., Donoho, 2006), and has been used to derive the coseismic radiation during great earthquakes in subduction zones (Yao et al., 2011, 2013; Yin et al., 2016). Compared with the widely used finite fault slip inversion methods, most of which use the low-frequency data and cannot easily resolve the details in high frequencies, the CS method is carried out in the frequency domain based on sparsity-constraint inversion, and is able to directly give spatial and temporal distribution of coseismic radiation at high and intermediate frequencies (e.g., 0.05–1 Hz) projected on the focal plane without prior assumptions on fault geometry and certain rupture parameters (Yao et al., 2011; Yin and Yao, 2016).

The CS method can be summarized as solving the following optimization problem:

$$\bar{\mathbf{X}}(\omega) = \operatorname{argmin}(\|\mathbf{B}(\omega) - \mathbf{A}(\omega)\mathbf{X}(\omega)\|_1 + rN\|\mathbf{X}(\omega)\|_1), \quad (1)$$

where  $\mathbf{X}(\omega)$  is the source radiation distribution vector at the angular frequency of  $\omega$ .  $\mathbf{A}(\omega)$  is the transmission matrix,

$\mathbf{B}(\omega)$  is the observed data spectral vector for all  $N$  stations within each sliding time window, and  $r$  is the damping factor ( $r=0.4$  in this study) (see Yin and Yao, 2016 for details). After we estimated coseismic sources  $\bar{\mathbf{X}}(\omega)$  at each frequency using the Disciplined Convex Programming (<http://cvxr.com>), we remove unreliable results with large data fitting errors ( $\|\mathbf{B}(\omega) - \mathbf{A}(\omega)\mathbf{X}(\omega)\|_1 / \|\mathbf{A}(\omega)\mathbf{X}(\omega)\|_1 > 30\%$  for LF results, and  $> 40\%$  for the HF results), which are due to the incoherent waveforms within corresponding time windows, in particular after 50 s (Figure 3a and b). Finally, the results at different frequencies are smoothed using a Gaussian function (Yao et al., 2011) with the smoothing radius of 15 km and are then averaged to give the final spatial and temporal distribution of seismic radiation in two different frequency bands of 0.05–0.3 Hz (LF) and 0.3–0.6 Hz (HF) (Figure 3c and d).

### 3.3 Shear stress change calculation

Moreover, we calculate static coseismic shear stress drop distribution of this event based on the slip inversion results (Avouac et al., 2015). The static shear stress drop is one of the fundamental parameters related to earthquake rupture dynamics (Allmann and Shearer, 2009; Noda et al., 2013). It can be estimated from the seismic moment and fault geometry/dimensions (e.g. Kanamori and Anderson, 1975; Parsons et al., 1988) or analytically calculated from the coseismic

slip distribution based on half-space solutions (e.g. Okada, 1992). Here we calculate the static shear stress drop from slip distribution using the finite-element software-Pylith (Aagaard et al., 2013), which can incorporate heterogeneous material properties. Our model domain is set as large as 400 km×300 km×100 km to avoid numerical boundary effects. The boundary conditions are set as fixed normal to the boundary surface and free slip in other directions, following our previous approach (Yin et al., 2016). Other structural information, such as density  $\rho$ , Lamé constant  $\lambda$ , shear modulus  $\mu$ , and Poisson's ratio  $\nu$  are derived from a 1D layered regional model (see Table 1 and Galetzka et al., 2015).

### 3.4 CS resolution tests

Before applying the CS method to the real data, we design a series of resolution tests to guarantee its capability to get robust results for this event. First we set the spike-source se-

ries using the stacked waveform of the first 10 seconds of the mainshock in three different rupture directions (see Figure 4; along-strike: green; perpendicular to strike: blue; oblique: red) to test the ability of the CS method with different source distributions. The recovered sources are nicely distributed along different directions except some minor smearing effects in the LF band between two nearby sources (Figure 4a). This is due to the sliding time window truncation of the waveform with longer wavelength, but it does not affect the overall patterns of the radiation sources during the earthquake rupture in different directions.

In the second test, we investigate the influences on the CS results from depth phases (e.g. pP, sP) using synthetic waveforms generated from the first 20-second waveform of a nearby  $M_w$  6.8 aftershock on April 26, 2015 (Figure 5c and d), which can be approximated as a point source compared with the mainshock. Another reason why we choose this aftershock is that this event presents striking similarities

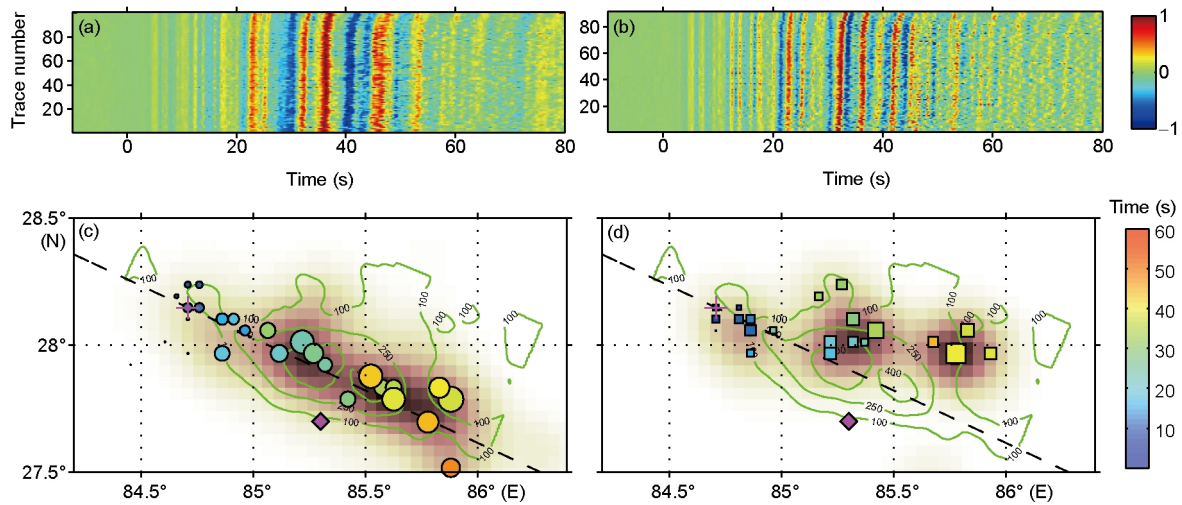


**Figure 3** Bandpass filtered P waveforms after alignment for the stations used in this study in the low frequency band of 0.05–2 Hz (a) and the high frequency band of 0.2–4 Hz (b). (c) and (d) show the spatiotemporal distribution of coseismic radiation sources of the Nepal  $M_w$  7.8 event from CS in the low frequency band of 0.05–0.3 Hz (circles) and high frequency band of 0.3–0.6 Hz (squares), respectively. The size and color of symbols indicate the relative power and source time of seismic radiation, respectively. Background image shows the normalized total radiation power in each frequency band and green contours indicate the slip distribution (cm, also shown in Figure 7) from Avouac et al. (2015). The purple cross indicates the epicenter of the mainshock. The purple diamond denotes the position of Kathmandu.

**Table 1** Parameter-settings of the 1-D layered model for the shear stress change calculation

Thickness $dZ$ (km)	P velocity $V_P$ (km s <sup>-1</sup> )	S velocity $V_S$ (km s <sup>-1</sup> )	Density $\rho$ (kg m <sup>-3</sup> )	Lamé constant $\lambda$ (GPa)	Shear modulus $\mu$ (GPa)	Poisson's ratio $\nu$
4.00	5.5	3.20	2.53	24.7	25.9	0.24
12.00	5.85	3.40	2.64	29.3	30.5	0.25
4.00	6.00	3.50	2.69	30.9	33.0	0.24
6.50	6.45	3.70	2.83	40.2	38.7	0.25
10.00	6.65	3.85	2.90	42.3	43.0	0.25
5.00	7.20	4.15	3.07	53.4	52.9	0.25
14.00	7.50	4.20	3.17	66.5	55.9	0.27
–	7.90	4.30	3.30	83.9	61.0	0.29

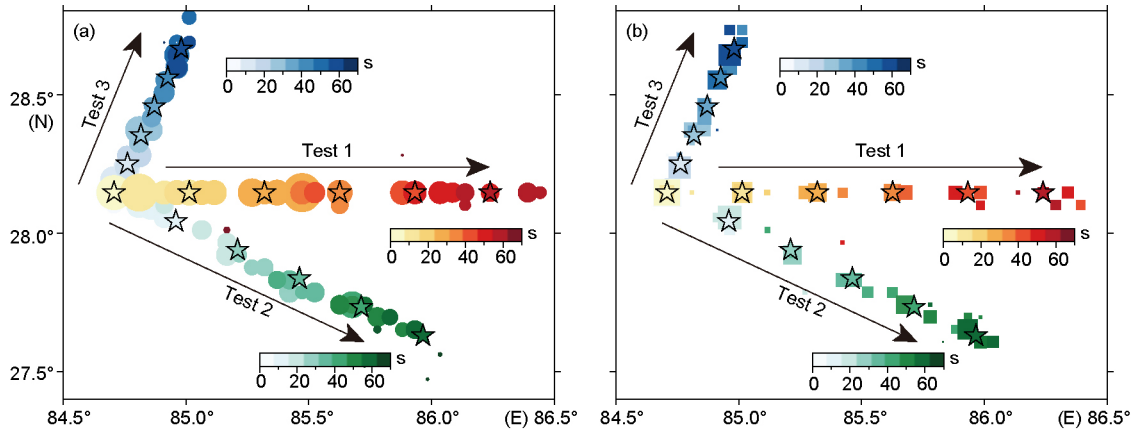


**Figure 4** Results of synthetic resolution tests for rupture along different directions (along-strike: green; perpendicular to strike: blue; oblique: red). Stars represent the synthetic spike sources. (a) Recovered CS results in the low frequency band (0.05–0.3) Hz (circles); (b) recovered CS results in the high frequency band (0.3–0.6) Hz (squares). Here each test in (a) or (b) is conducted separately but the results are plotted on the same figure. The color of all symbols indicates the source time of the synthetic or the recovered sources.

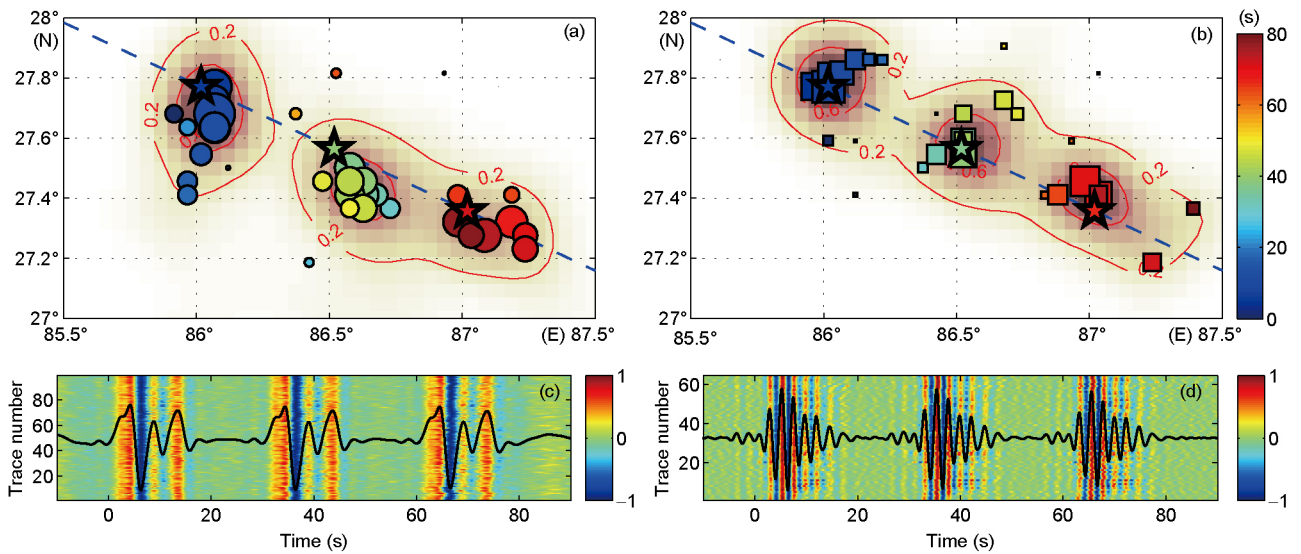


**Figure 5** Results of synthetic resolution tests using the waveforms of the  $M_w$  6.8 aftershock. (a) Recovered CS results in the low frequency band (0.05–0.3) Hz (circles); (b) recovered CS results in the high frequency band (0.3–0.6) Hz (squares). Stars represent the synthetic sources. The background image as well as the contours indicate the normalized total radiation power in each frequency band. The color of all symbols indicates the source time of the synthetic sources or the recovered sources. (c) and (d) show the synthetic waveforms at each station and their stacked waveforms (black) in the low and high frequency bands, respectively.

during the onset phase (first 20–25 s) of the waveforms with the mainshock (Denolle et al., 2015). The recovery of these synthetic sources is quite good in both LF and HF bands, despite there are small artifacts resulted from the truncation of waveforms as well as from the depth phases (Figure 5a and b). We also find that, because this  $M_w$  7.8 Nepal event has a relatively shallow focal depth (<15 km), the influences from depth phases on the CS results seem less severe than the 2015 Illapel, Chile earthquake (Yin et al., 2016).

#### 4. Results

Our CS results indicate a unilateral rupture process in both

low and high frequency bands for the 2015  $M_w$  7.8 Nepal earthquake (Figure 3c and d). In the LF band (0.05–0.3 Hz), most coseismic radiation occurs about 50 km and 100 km southeast of the epicenter at ~25 s and ~40 s, respectively (Figures 3c and 6a). For the HF band (0.3–0.6 Hz), energy radiation distributes around three clusters: close to hypocenter within the 5–15 s, 50 km east within 20–30 s, and 100 km within 35–45 s east of the epicenter, respectively (Figures 3d and 6b). Our results show that the main rupture process has a duration of ~50 s, which can also be seen from similarities of the aligned waveforms considering the propagation directivity. We can also estimate the average rupture speed by approximating the rupture front from the LF results (Figure 6a).

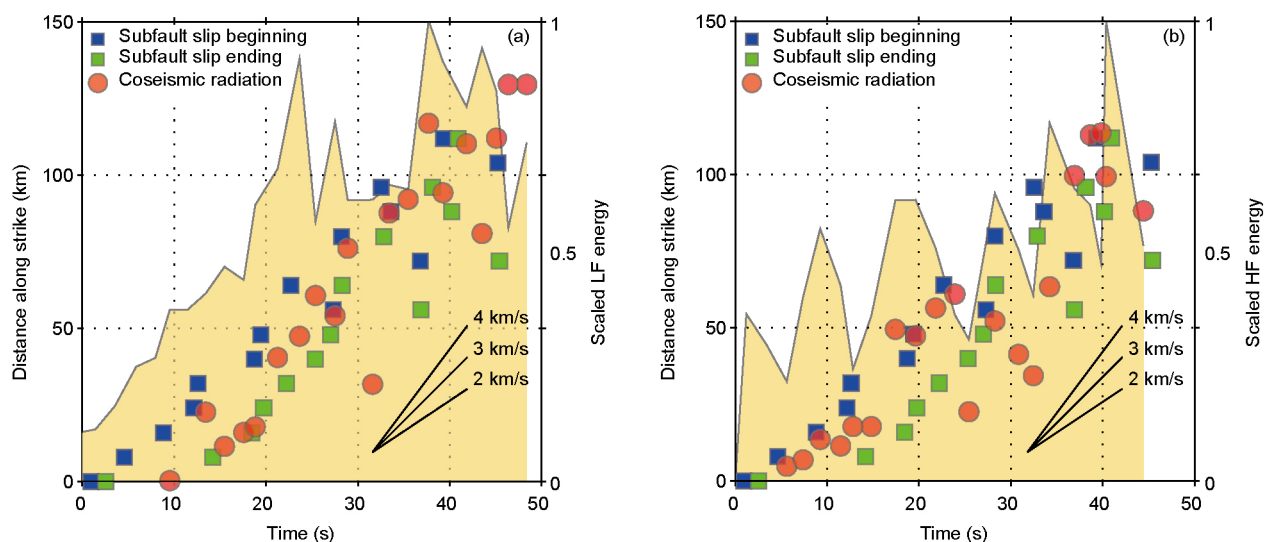


**Figure 6** Along-strike rupture speed estimation from (a) the low frequency sources of seismic radiation and (b) the high frequency sources of seismic radiation (red circles; from Figure 3), compared with the slip inversion results (Avouac et al., 2015). Blue and green squares represent the starting and ending times of the slip on each subfault in the slip model with respect to the hypocentral time, respectively. Gray curves with yellow shading show the scaled radiated energy (to their maxima, respectively) within different frequency bands. X-axis represents the time of seismic radiation and slip. Left y-axis is the distance along strike from the epicenter and right y-axis shows the scaled energy.

The rupture propagates at  $\sim 3 \text{ km s}^{-1}$ , well consistent with the speed estimation from the slip inversion results (Avouac et al., 2015). However, it is hard to give a very stable estimation on the rupture speed from HF results due to the clustering pattern of HF results (Figure 6b). Using the well-determined HF subevents from backprojection analysis, the along strike rupture speed is about  $2.8 \text{ km s}^{-1}$  (Qin and Yao, 2017).

Furthermore, we calculate and compare the distribution of shear stress change (negative static coseismic stress drop, see Figure 7a and c) with the coseismic radiation. The overall pattern of shear stress change distribution is similar to the slip distribution. Most of the negative regions are constrained within the large slip region ( $>2 \text{ m}$ ) (red region in Figure 7a and c), where accumulated elastic stress has been released during the earthquake rupture. In contrast, the positive regions (blue region in Figure 7a and c) correspond to regions with little slip and at the boundary of large slip, indicating that these regions have been loaded. Note that the peaks of the coseismic shear stress change are not exactly corresponding to the peaks of coseismic slip but are located at the region where the slip gradient is largest (e.g. Yang et al., 2012a; Yin et al., 2016; He et al., 2016). This pattern is also consistent with the elastic stress-strain relation in the analytical solution.

Combining all these comparable results, there shows an obvious pattern of the distribution of coseismic radiation sources in different frequency bands. The LF radiation mainly overlaps within the large slip area (slip  $> 1 \text{ m}$ ; from Avouac et al., 2015; Figure 3c), well corresponding to the negative coseismic shear stress change region (Figure 7a). Although the slip model indicates two peaks with slip more than  $4 \text{ m}$ , our LF coseismic radiation sources do not directly

overlap with the slip peaks but are located at their boundaries, where the peaks of stress drops are.

On the other hand, HF radiation is mainly originated from down-dip area around the margin of the large slip area (Avouac et al., 2015; Figure 3d). Compared with the stress change distribution, most of these HF radiation sources are located in the positive stress change or the transition region between positive and negative stress changes (Figure 7c). The positive stress change indicates that these regions have been loaded during the rupture, thus our results show the correspondence between HF radiation sources and coseismic loading. The differences between LF and HF results indicate frequency-dependent rupture characteristics along the dip direction in the continent-continent collisional environment.

## 5. Discussion

### 5.1 Coseismic energy radiation of the Nepal earthquake

In order to exclude the potential bias in our comparison with the slip model from Avouac et al. (2015), we also compare our results with other published slip models (e.g. Galetzka et al., 2015; Grandin et al., 2015; Lindsey et al., 2015; Wang and Fialko, 2015; Yue et al., 2016). All of these models show strikingly similar slip distributions except the slight difference in the maximum slip. All models indicate that the mainshock rupture extends  $140 \text{ km}$  along strike and  $70 \text{ km}$  along dip. The further downdip rupture propagation feature (with smaller slip of  $\sim 2\text{--}3 \text{ m}$ ) is located between our two HF energy clusters at  $20\text{--}30 \text{ s}$  and  $35\text{--}45 \text{ s}$  (Figure 3c and d). More intriguingly, most of these models present the two peaks of

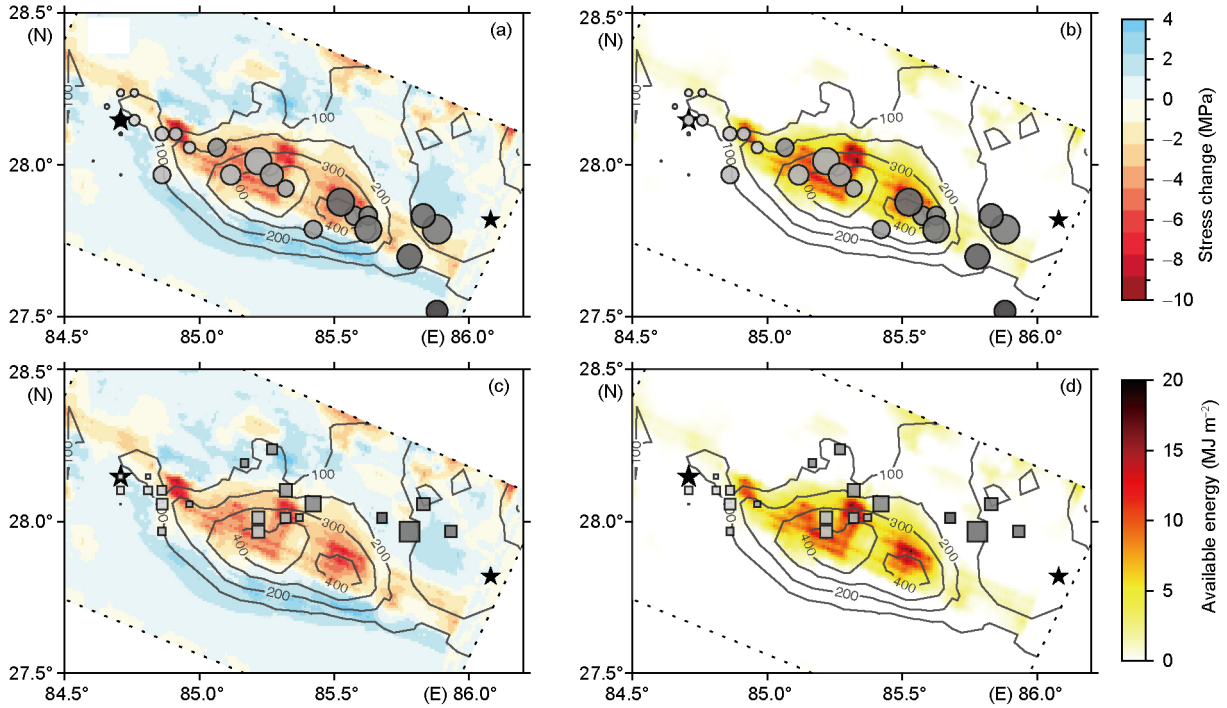


**Figure 7** Comparisons between low frequency seismic radiation results (circles) with coseismic shear stress change (a) and distribution of available energy (b). (c) and (d) are for high frequency seismic radiation results (squares). Black stars show the epicenters of the  $M_w$  7.8 mainshock and the largest aftershock ( $M_w$  7.2). Contours represent the coseismic slip distribution of the mainshock from Avouac et al. (2015).

large slip distribution ( $>5$  m for these results) in almost the same locations (e.g. Galetzka et al., 2015; Grandin et al., 2015; Lindsey et al., 2015; Yue et al., 2016). The similarity among these slip models further confirms the reliability of comparisons between our observed frequency-dependent radiation and the slip distribution patterns.

The frequency-dependent coseismic radiation has been observed for a few megathrust earthquakes in the subduction zones, e.g. the 2004 Sumatra  $M_w$  9.2, the 2005 Sumatra  $M_w$  8.6, the 2010 Maule  $M_w$  8.8, the 2011 Tohoku  $M_w$  9.0, and the 2015 Illapel  $M_w$  8.3 earthquakes (Wang and Mori, 2011; Lay et al., 2012; Yao et al., 2011, 2013; Yin et al., 2016). Our results show that the frequency-dependent coseismic radiation not only exists in oceanic subduction zones, but also in the continent-continent collisional environment. Such feature has been attributed to depth-varying frictional properties on the megathrust, in which the LF coseismic radiation corresponds to the large slip region while the HF energy is emitted from isolated patches downdip to the large asperity (Lay et al., 2012). Furthermore, coseismic shear stress changes computed from slip distributions of the 2015 Illapel earthquake have shown that the LF radiation is mainly associated with regions with negative shear stress changes and the HF energy mainly from deeper portion of the slab with positive shear stress changes (Yin et al., 2016). Our results of the 2015  $M_w$  7.8 Nepal earthquake have also shown systematic correspondence between coseismic radiation in different frequency bands and the coseismic stress changes, suggesting

that the HF radiations are emitted from the down-dip small asperities. These small patches are loaded due to the rupture of shallower large slip regions. In the Nepal section of the Himalaya thrust belt, our results have shown the similar pattern (Figure 7a and c) to that of the 2015 Illapel earthquake and thus provide another evidence for the relation between stress status and coseismic radiation energy, in addition to megathrust earthquakes. Furthermore, these results provide us an improved interpretation of frequency-dependence in subduction zones (Lay et al., 2012; Yao et al., 2013).

In order to further understand the physical mechanism on the frequency-dependent coseismic radiation, we calculate the available energy distribution using the slip distribution and stress drop. The available energy density  $E_{T0}$  equals to the released elastic energy minus frictional energy, i.e., the summation of radiated seismic  $E_R$  and fracture energy  $E_G$  (Kanamori and Rivera, 2006):

$$(E_{T0})_i = (E_R + E_G)_i = \frac{1}{2}(\tau_0 - \tau_d)_i D_i A = -\frac{1}{2} \Delta\tau_i D_i A, \quad (2)$$

where the subscript  $i$  means the  $i$ th subfault in the slip model. The parameters  $\tau_0$  and  $\tau_d$  are the shear stress before and after an earthquake.  $D_i$ ,  $\Delta\tau_i$  and  $A$  are the slip, shear stress change and area of the  $i$ th subfault, respectively. For regions with large slip, the distribution of available energy is similar to the coseismic stress drop (Figure 7). In contrast, the calculated energy is close to zero for regions with little coseismic slip, although coseismic stress changes are nonzero.

Based on the earthquake energy partitioning in the slip-

weakening model (Ida, 1972; Andrews, 1976), the seismic moment  $M_0$  released during an earthquake can be divided into 3 parts: the frictional energy, radiated energy  $E_R$  and fracture energy  $E_G$ . The fracture energy is the sum of all kinds of energies associated with faulting, and is closely related to the critical slip-weakening distance ( $D_c$ ). The value of  $D_c$  has been mostly regarded as a constant in numerical simulations (e.g. Andrews, 1976; Mai et al., 2006; Yang et al., 2013; Weng et al., 2015, 2016), but has also been suggested proportional to the final slip (e.g. Tinti et al., 2005). More recently, the  $D_c$  value has been suggested to decrease with depth in subduction zones (Yang and Weng, 2016). From the coseismic slip model, we can get the available energy distribution  $E_{T0}$ , which includes  $E_R$  and  $E_G$ . Because the fracture energy  $E_G$  is hard to estimate from seismic observations, we cannot completely separate the radiated energy from  $E_{T0}$ . However, the radiated energy is positively related to the  $E_{T0}$  in either cases of  $D_c$  value (constant or proportional to final slip) based on the representative slip weakening model (Andrews, 1976), so we can use distribution of available energy to constrain the radiated energy distribution, especially the LF radiation from our results (Figures 3c, 7a and 7b).

The LF radiation bursts are well correlated with regions of large available energy (Figure 7b). Most of the energy is released during 20–30 s and 35–45 s (Figure 6), consistent with the results from spectral analysis of teleseismic waves (Denolle et al., 2015). These different kinds of observations provide us important clues to infer and understand the dynamic features of large earthquakes from the CS method. In comparison, our HF radiation sources are mostly located at regions where the available energy is close to zero because of little slip or near-zero stress change. Since these regions are mostly associated with positive shear stress changes (Figure 7c), our results suggest that the HF coseismic radiations may originate from small-scale asperities, which are loaded to failure during the mainshock and emitting HF signals (e.g. Yin et al., 2016).

## 5.2 Frequency-dependent seismic radiation in the Nepal segment of MHT

Combining our results with the slip inversion model (Avouac et al., 2015), inferred stress change/available energy distribution (Figure 7), and the aftershock distribution, the 2015 Nepal earthquake sequence appears to be well consistent with the seismic asperity model (Figure 8). Both of our LF results (Figure 3c) and the shear stress change distribution (Figure 7a) inferred from slip model (mainly based on LF data) illustrate the existence of a large asperity along the strike direction of the MHT, which has been ruptured during the mainshock and released most of the accumulated elastic energy (Figure 7b and d). This large asperity represents stress accumulation in depth that is also shown by the locking distribution of the

MHT from the surface to the depth of 15 to 20 km (Mugnier et al., 2011; Ader et al., 2012).

Our results clearly show frequency-dependent variations of rupture characteristics in the Nepal segment of the Himalayan continental thrust belt (Figures 3, 6, and 8), similar to the findings of a few great earthquakes in subduction zones (Yao et al., 2011, 2013; Lay et al., 2012; Yin et al., 2016). For megathrust earthquakes, HF radiation appears to be systematically deeper than LF radiation, which is interpreted to occur mainly in the conditionally stable region at depths of 30–45 km on the subduction interface (Lay et al., 2012; Yao et al., 2013; Yin et al., 2016). This depth corresponds to the onset of plasticity of feldspar in basalt of the oceanic plate at about 450°C (Scholz, 1998) or intersection of continental Moho with the megathrust (Oleskevich et al., 1999). However, beneath the Himalayas, this transition depth becomes much shallower, 15–20 km corresponding to the onset of plasticity of quartz for continental crust at about 300°C (Scholz, 1998). For the 2015 Nepal event, the clusters of HF radiation appear in the down-dip region compared to the LF radiation. As we use teleseismic P waves, our results do not have depth resolution of seismic radiation sources. However, if we assume the sources are generated from the MHT fault interface, the HF radiation appears to originate mainly from the deeper boundary of large coseismic slip regions at around 15–20 km depth, at which previous studies indicate a transition from velocity weakening to stable sliding (Cattin and Avouac, 2000; Avouac, 2003). The transition in frictional properties might generate small-scale asperities (Figure 8), which are loaded to failure during the mainshock, producing HF radiation.

In addition, in some subduction zones such as Japan or Sumatra, it has been documented that fault patches breaking in  $M7-8$  events are capable of failing again in giant  $M9$  earthquakes that rupture multiple segments (Sieh et al., 2008). The 1344 or 1408 earthquake might have ruptured the 2015 mainshock area and the neighboring section in the west (Bollinger et al., 2016). However, in the Himalaya arc overlapping rupture areas of different large earthquakes ( $M > 8$ ) seem not quite common since 1500 (Figure 1) (Bilham et al., 2001; Bilham and Ambraseys, 2005; Feldl and Bilham, 2006). Although it might be limited by the short observational history, such segmented rupture behaviors may reflect differences of tectonic settings and seismogenic mechanisms between oceanic subduction zones and continental collision zones despite that similar frequency-dependent coseismic radiations are observed.

## 5.3 Correlation among frequency-dependent radiation, frictional properties, and other geophysical observations

The 2015 Nepal earthquake locates in the Nepal segment with complex tectonic interactions. Beneath the Himalayan thrust belt, the MHT can be divided into 3 different down-dip

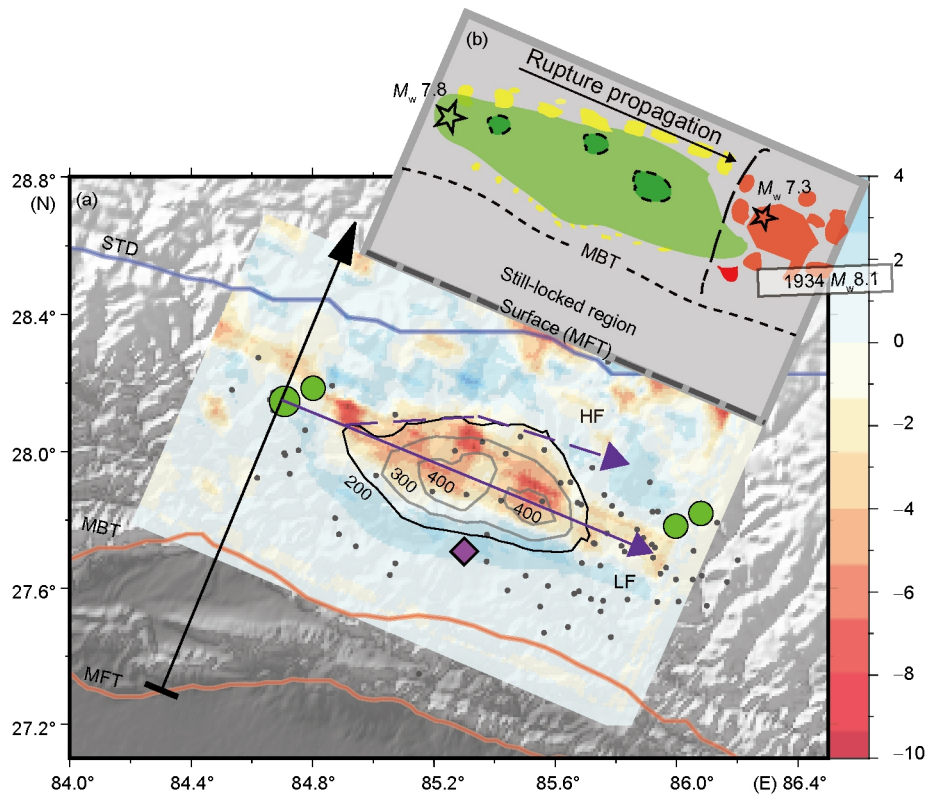


**Figure 8** Integrated results and the schematic asperity distribution for this earthquake sequence. (a) Black dots show the aftershocks until May 12, 2015, and green circles represent the mainshock and three largest aftershocks of  $M_w$  6.6, 6.7 and 7.3. Background image shows the coseismic shear stress change with coseismic slip contours in cm. Two purple arrows show the track of low frequency (LF) and high frequency (HF) radiation, respectively, and the black arrow indicates the profile shown in Figure 9. The purple diamond denotes the location of Kathmandu. (b) Schematic distribution of seismic asperities inferred from our results, slip inversion results, and aftershock distribution (yellow and red). The mainshock rupture area is shown in green. The dashed dark green region shows the region with large negative shear stress change. The bold dashed line indicates the approximate western end of rupture area of the 1934  $M_w$  8.1 event (Bilham and Ambraseys, 2005).

regimes: the brittle failure regime in the upper-mid crust (<15 km) beneath the Outer Himalaya and the Lesser Himalaya, the brittle-ductile transitional regime at the depth of about 15–20 km beneath the Higher Himalaya, and the creep regime (>20 km) beneath the Tethys Himalaya (Figure 9).

The Outer and Lesser Himalaya regions have a low interseismic uplift rate (Jackson and Bilham, 1994) and low horizontal velocity relative to the Indian plate from GPS observations (Bilham et al., 1997; Jouanne et al., 1999; Larson et al., 1999). The high interseismic coupling (ISC) distribution (Ader et al., 2012), occurrence of great historical earthquakes, and large coseismic slip and stress release for the 2015 Nepal event (Figure 7) indicate that the shallower part of the MHT fault interface (above about 15 km depth) shows the typical stick-slip behavior, i.e., accumulation of large elastic strain during the interseismic period and then release of the accumulated strain and shear stress through large coseismic slip and LF radiation (Figure 9).

At depths of 10–30 km beneath the Higher Himalaya there exists a region with highly clustered micro-seismicity (Figure 9), which are almost continuously distributed along the strike of the Himalayan arc (Pandey et al., 1995, 1999). Fur-

thermore, results from magnetotelluric sounding (Lemonnier et al., 1999; Unsworth et al., 2005; Patro and Harinarayana, 2009) indicate that there exists an obvious high-conductivity structure at about 15–20 km depth. This high conductivity structure, well corresponding to the thermal structure (Henry et al., 1997; Royden et al., 1997; Cattin and Avouac, 2000), has been interpreted as the presence of fluids released by metamorphic reactions (Avouac, 2003). Receiver function imaging from HI-CLIMB experiment (Nábělek et al., 2009) suggested a discontinuous interface with sharp velocity decrease around the focal depth of this Nepal event (~21 km; He et al., 2015), implying the existence of fluids. Based on the results from ambient noise tomography near this region, both the shear wave velocity images and radial anisotropy indicate clear structural differences around the hypocenter region (Guo et al., 2009, 2012). All of these structural differences in this transitional zone might be responsible for the formation of small scale asperities accompanied with stress accumulation from plate convergence. These small asperities are loaded to failure, thus radiating HF energy as shown in our CS results (Figure 3).

The deeper part of MHT (>20 km depth and beneath Tethys

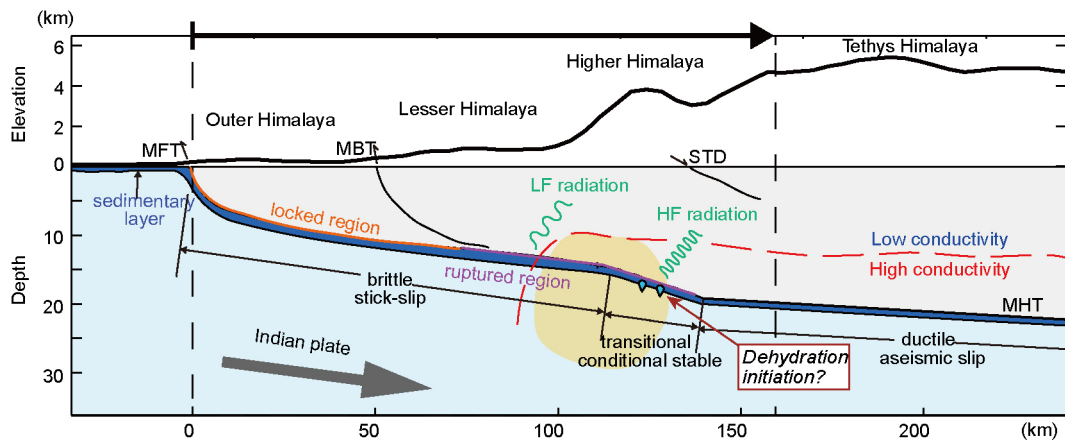


**Figure 9** Schematic cross-section view of the Himalayan thrust fault system across the epicenter (location shown in Figure 8) showing the downdip variations of fault frictional properties and possible seismogenic mechanism of this event. The fault geometry is inferred from Pandey et al. (1995) and Bollinger et al. (2004). The yellow area indicates the region with high micro seismicity (Pandey et al., 1995, 1999). The red dashed line gives the approximate upper boundary of the high conductivity structure from MT observations (Lemonnier et al., 1999). The gray arrow indicates the direction of the Indian plate subduction. The x-axis gives the distance along the profile of the MFT and the y-axis shows the surface topography (upper part) and the depth (lower part).

Himalaya) is characterized by the ductile shear zone with aseismic slip, high inelastic deformation rate, and comparatively higher temperature  $> 350^{\circ}\text{C}$  (Cattin and Avouac, 2000; Ader et al., 2012), at which quartzo-feldspathic rocks transform from frictional sliding to stable creep in laboratory experiments (Blanpied et al., 1995; Marone, 1998).

The effect of the stress transfer between these three portions can be illustrated using a simplified spring-and-slider model as shown by Avouac (2003). Combine all of these observations and our coseismic radiation results, we propose one possible seismogenic mechanism of the 2015  $M_w$  7.8 Nepal event (Figure 9): sufficient stress and strain have been accumulated during the interseismic cycle as the result of convergence between the Indian plate and the Tibetan Plateau, which forms a relatively uniform and large scale asperity on the brittle part of the MHT. Dehydration process may occur at the depth of  $\sim 15\text{--}20$  km (see Figure 9) and aqueous fluids are trapped in the lower end of the brittle part of MHT, which then results in increased pore pressure and decreased mechanic strength of the fault. This process could contribute to the initiation of the rupture that finally developed into the devastating event on April 25, 2015.

However, all the present observations suggest that the 2015 event has not caused noticeable surface ruptures, therefore resulting in much smaller surface damages compared to the 2008  $M_w$  7.9 Wenchuan earthquake in the margin of southeastern Tibetan Plateau. From the slip inversion results and aftershock distribution (Figure 8), it appears that shallower part of the MHT fault interface beneath the outer Himalayan (between MFT and MBT) is still locked and could potentially evolve into another devastating earthquake in the future. Stopping of the rupture to the shallow MHT may be attributed to the geometrical and/or frictional heterogeneities, as shown in numerical simulations (Yang et al., 2012b, 2013).

Indeed, the Gorkha earthquake rupture has been suggested to be bounded by steeper ramps on the fault segment (Hubbard et al., 2016). In addition, the western Nepal section of the Himalayan thrust has been quiet for more than 500 years since the great 1505  $M_w$  8.2 earthquake. Considering 300–500 yr recurrence interval of about magnitude 8 earthquake in the Himalayan thrust belt (Liu et al., 2015), the western Nepal section of the Himalayan thrust may be near the end of earthquake cycle. Loading of the coseismic slip of the 2015 Nepal earthquake may further increase the seismic potential of western Nepal (Avouac et al., 2015).

## 6. Conclusion

We apply the compressive sensing method to track seismic radiation and rupture process during mainshock of the 2015 Nepal Gorkha  $M_w$  7.8 earthquake. The rupture process is unilateral, propagating from the epicenter to southeast with a relatively stable rupture speed of about  $3\text{ km s}^{-1}$ . In addition, the coseismic radiation of the 2015 Nepal earthquake shows distinct frequency-dependent feature: low-frequency radiation is in the shallow part and high-frequency radiation originates from the deeper portion of the ruptured plane. We calculate the coseismic shear stress changes and find that the frequency-dependent coseismic radiation sources are closely related to the stress variation status and frictional properties on the fault plane. We propose a seismic asperity model to interpret the 2015 Nepal earthquake sequence and compare its frequency-dependent coseismic radiation with that in megathrust events. Together with previous studies of this area, the seismogenic mechanism of this earthquake is related to the depth-varying frictional properties of the plate interface of the main Himalayan thrust system. Rupture initiation is likely due to dehydration-induced weakening of the fault interface

as integrated with other geophysical observations in this region. As inferred from the coseismic slip patterns and after-shock distribution, the shallower part of the MHT fault beneath the outer Himalayan is still locked and may evolve into another devastating earthquake in the future.

**Acknowledgements** We thank An Yin, Mike Taylor and Zhi Guo for providing the fault line data of the Tibetan plateau, Shengji Wei for sharing the slip inversion model, and the reviewers for their comments to improve this manuscript. All the waveform data are obtained from the Data Management Center (DMC) of the Incorporated Research Institutions of Seismology (IRIS), and some of the figures are made by the Generic Mapping Tools (GMT) (<http://gmt.soest.hawaii.edu/>). This work was supported by National Natural Science Foundation of China (Grant Nos. 41374055, 41225010), Chinese University of Hong Kong Direct Grant for Research (Grant No. 3132771), HKSAR Research Grant Council ECS (Grant No. 2191093) and GRF (Grant No. 2130509), and the Fundamental Research Funds for the Central Universities (Grant No. WK2080000053).

## References

- Aagaard B T, Knepley M G, Williams C A. 2013. A domain decomposition approach to implementing fault slip in finite-element models of quasi-static and dynamic crustal deformation. *J Geophys Res-Solid Earth*, 118: 3059–3079
- Ader T, Avouac J P, Liu-Zeng J, Lyon-Caen H, Bollinger L, Galetzka J, Genrich J, Thomas M, Chanard K, Sapkota S N, Rajaure S, Shrestha P, Ding L, Flouzat M. 2012. Convergence rate across the Nepal Himalaya and interseismic coupling on the main Himalayan thrust: Implications for seismic hazard. *J Geophys Res*, 117: B04403
- Allmann B P, Shearer P M. 2009. Global variations of stress drop for moderate to large earthquakes. *J Geophys Res*, 114: B01310
- Andrews D J. 1976. Rupture propagation with finite stress in antiplane strain. *J Geophys Res*, 81: 3575–3582
- Avouac J P. 2003. Mountain building, erosion, and the seismic cycle in the Nepal Himalaya. *Adv Geophys*, 46: 1–80
- Avouac J P, Meng L, Wei S, Wang T, Ampuero J P. 2015. Lower edge of locked main Himalayan thrust unzipped by the 2015 Gorkha earthquake. *Nat Geosci*, 8: 708–711
- Bettinelli P, Avouac J P, Flouzat M, Jouanne F, Bollinger L, Willis P, Chitrakar G R. 2006. Plate motion of India and interseismic strain in the Nepal Himalaya from GPS and DORIS measurements. *J Geodesy*, 80: 567–589
- Bilham R, Ambraseys N. 2005. Apparent Himalayan slip deficit from the summation of seismic moments for Himalayan earthquakes, 1500–2000. *Curr Sci*, 88: 1658–1663
- Bilham R, Larson K, Freymueller J. 1997. GPS measurements of present-day convergence across the Nepal Himalaya. *Nature*, 386: 61–64
- Bilham R, Gaur V K, Molnar P. 2001. Earthquakes: Himalayan seismic hazard. *Science*, 293: 1442–1444
- Blanpied M L, Lockner D A, Byerlee J D. 1995. Frictional slip of granite at hydrothermal conditions. *J Geophys Res*, 100: 13045–13064
- Bollinger L, Avouac J P, Cattin R, Pandey M R. 2004. Stress buildup in the Himalaya. *J Geophys Res*, 109: B11405
- Bollinger L, Tapponnier P, Sapkota S N, Klinger Y. 2016. Slip deficit in central Nepal: Omen for a repeat of the 1344 AD earthquake? *Earth Planets Space*, 68: 12
- Cattin R, Avouac J P. 2000. Modeling mountain building and the seismic cycle in the Himalaya of Nepal. *J Geophys Res*, 105: 13389–13407
- DeMets C, Gordon R G, Argus D F, Stein S. 1994. Effect of recent revisions to the geomagnetic reversal time scale on estimates of current plate motions. *Geophys Res Lett*, 21: 2191–2194
- Denolle M A, Fan W, Shearer P M. 2015. Dynamics of the 2015  $M 7.8$  Nepal earthquake. *Geophys Res Lett*, 42: 7467–7475
- Donoho D L. 2006. Compressed sensing. *IEEE T Inform Theory*, 52: 1289–1306
- Fan W, Shearer P M. 2015. Detailed rupture imaging of the 25 April 2015 Nepal earthquake using teleseismic  $P$  waves. *Geophys Res Lett*, 42: 5744–5752
- Feldl N, Bilham R. 2006. Great Himalayan earthquakes and the Tibetan Plateau. *Nature*, 444: 165–170
- Galetzka J, Melgar D, Genrich J F, Geng J, Owen S, Lindsey E O, Xu X, Bock Y, Avouac J P, Adhikari L B, Upreti B N, Pratt-Sitaula B, Bhattarai T N, Sitaula B P, Moore A, Hudnut K W, Szeliga W, Normandeau J, Fend M, Flouzat M, Bollinger L, Shrestha P, Koirala B, Gautam U, Bhattarai M, Gupta R, Kandel T, Timsina C, Sapkota S N, Rajaure S, Maharjan N. 2015. Slip pulse and resonance of the Kathmandu basin during the 2015 Gorkha earthquake, Nepal. *Science*, 349: 1091–1095
- Grandin R, Vallée M, Satriano C, Lacassin R, Klinger Y, Simoes M, Bollinger L. 2015. Rupture process of the  $M_w=7.9$  2015 Gorkha earthquake (Nepal): Insights into Himalayan megathrust segmentation. *Geophys Res Lett*, 42: 8373–8382
- Guo Z, Gao X, Yao H, Li J, Wang W. 2009. Midcrustal low-velocity layer beneath the central Himalaya and southern Tibet revealed by ambient noise array tomography. *Geochem Geophys Geosyst*, 10: Q05007
- Guo Z, Gao X, Wang W, Yao Z. 2012. Upper- and mid-crustal radial anisotropy beneath the central Himalaya and southern Tibet from seismic ambient noise tomography. *Geophys J Int*, 189: 1169–1182
- He X, Ni S, Ye L, Lay T, Liu Q, Koper K D. 2015. Rapid seismological quantification of source parameters of the 25 April 2015 Nepal Earthquake. *Seismol Res Lett*, 86: 1568–1577
- He B, Yang H, Weng H. 2016. Rupture process of the 2012 Nicoya earthquake inferred from interseismic locking distributions. In: 2016 AOGS Annual Meeting Abstracts
- Henry P, Le Pichon X, Goffé B. 1997. Kinematic, thermal and petrological model of the Himalayas: Constraints related to metamorphism within the underthrust Indian crust and topographic elevation. *Tectonophysics*, 273: 31–56
- Hubbard J, Almeida R, Foster A, Sapkota S N, Bürgi P, Tapponnier P. 2016. Structural segmentation controlled the 2015  $M_w$  7.8 Gorkha earthquake rupture in Nepal. *Geology*, 44: 639–642
- Ida Y. 1972. Cohesive force across the tip of a longitudinal-shear crack and Griffith's specific surface energy. *J Geophys Res*, 77: 3796–3805
- Ishii M, Shearer P M, Houston H, Vidale J E. 2005. Extent, duration and speed of the 2004 Sumatra-Andaman earthquake imaged by the Hi-Net array. *Nature*, 435: 933–936
- Jackson M, Bilham R. 1994. Constraints on Himalayan deformation inferred from vertical velocity fields in Nepal and Tibet. *J Geophys Res*, 99: 13897–13912
- Jouanne F, Mugnier J L, Pandey M R, Gamond J F, Le Fort P, Serrurier L, Vigny C, Avouac J P. 1999. Oblique convergence in the Himalayas of western Nepal deduced from preliminary results of GPS measurements. *Geophys Res Lett*, 26: 1933–1936
- Kanamori H, Anderson D L. 1975. Theoretical basis of some empirical relations in seismology. *Bull Seismol Soc Am*, 65: 1073–1095
- Kanamori H, Rivera L. 2006. Energy partitioning during an earthquake. *Earthq Radiated Energy Phys Faulting*. AGU Geophys Monograph Ser, 70: 3–13
- Larson K M, Bürgmann R, Bilham R, Freymueller J T. 1999. Kinematics of the India-Eurasia collision zone from GPS measurements. *J Geophys Res*, 104: 1077–1093
- Lay T. 2015. The surge of great earthquakes from 2004 to 2014. *Earth Planet Sci Lett*, 409: 133–146
- Lay T, Kanamori H, Ammon C J, Koper K D, Hutko A R, Ye L, Yue H, Rushing T M. 2012. Depth-varying rupture properties of subduction zone megathrust faults. *J Geophys Res*, 117: B04311

- Lemonnier C, Marquis G, Perrier F, Avouac J P, Chitrakar G, Kafle B, Sapkota S, Gautam U, Tiwari D, Bano M. 1999. Electrical structure of the Himalaya of central Nepal: High conductivity around the mid-crustal ramp along the MHT. *Geophys Res Lett*, 26: 3261–3264
- Lindsey E O, Natsuaki R, Xu X, Shimada M, Hashimoto M, Melgar D, Sandwell D T. 2015. Line-of-sight displacement from ALOS-2 interferometry:  $M_w$  7.8 Gorkha Earthquake and  $M_w$  7.3 aftershock. *Geophys Res Lett*, 42: 6655–6661
- Liu J, Ji C, Zhang J Y, Zhang P Z, Zeng L S, Li Z F, Wang W. 2015. Tectonic setting and general features of coseismic rupture of the 25 April, 2015  $M_w$  7.8 Gorkha, Nepal earthquake. *Chin Sci Bull*, 60: 2640–2655
- Mai P M, Somerville P, Pitarka A, Dalguer L, Song S, Beroza G, Miyake H, Irikura K. 2006. On scaling of fracture energy and stress drop in dynamic rupture models: Consequences for near-source ground-motions. *Earthq Radiated Energy Phys Faulting*. American Geophysical Union. 283–293
- Marone C. 1998. Laboratory-derived friction laws and their application to seismic faulting. *Annu Rev Earth Planet Sci*, 26: 643–696
- Meng L, Zhang A, Yagi Y. 2016. Improving back projection imaging with a novel physics-based aftershock calibration approach: A case study of the 2015 Gorkha earthquake. *Geophys Res Lett*, 43: 628–636
- Molnar P, Stock J M. 2009. Slowing of India's convergence with Eurasia since 20 Ma and its implications for Tibetan mantle dynamics. *Tectonics*, 28: TC3001
- Mugnier J L, Huyghe P, Gajurel A P, Upreti B N, Jouanne F. 2011. Seismites in the Kathmandu basin and seismic hazard in central Himalaya. *Tectonophysics*, 509: 33–49
- Nábelek J, Hetényi G, Vergne J, Sapkota S, Kafle B, Jiang M, Su H, Chen J, Huang B S, Huang B S. 2009. Underplating in the Himalaya-Tibet collision zone revealed by the Hi-CLIMB experiment. *Science*, 325: 1371–1374
- Noda H, Lapusta N, Kanamori H. 2013. Comparison of average stress drop measures for ruptures with heterogeneous stress change and implications for earthquake physics. *Geophys J Int*, 193: 1691–1712
- Okada Y. 1992. Internal deformation due to shear and tensile faults in a half-space. *Bull Seismol Soc Am*, 82: 1018–1040
- Oleskevich D A, Hyndman R D, Wang K. 1999. The updip and downdip limits to great subduction earthquakes: Thermal and structural models of Cascadia, south Alaska, SW Japan, and Chile. *J Geophys Res*, 104: 14965–14991
- Pandey M R, Tandukar R P, Avouac J P, Lave J, Massot J P. 1995. Interseismic strain accumulation on the Himalayan crustal ramp (Nepal). *Geophys Res Lett*, 22: 751–754
- Pandey M R, Tandukar R P, Avouac J P, Vergne J, Héritier T. 1999. Seismotectonics of the Nepal Himalaya from a local seismic network. *J Asian Earth Sci*, 17: 703–712
- Parsons I D, Hall J F, Lyzenga G A. 1988. Relationships between the average offset and the stress drop for two- and three-dimensional faults. *Bull Seismol Soc Am*, 78: 931–945
- Patro P K, Harinarayana T. 2009. Deep geoelectric structure of the Sikkim Himalayas (NE India) using magnetotelluric studies. *Phys Earth Planet Inter*, 173: 171–176
- Qin W, Yao H. 2017. Characteristics of subevents and three-stage rupture processes of the 2015  $M_w$  7.8 Gorkha Nepal earthquake from multiple-array back projection. *J Asian Earth Sci*, 133: 72–79
- Royden L H, Burchfiel B C, King R W, Wang E, Chen Z, Shen F, Liu Y. 1997. Surface deformation and lower crustal flow in Eastern Tibet. *Science*, 276: 788–790
- Scholz C H. 1998. Earthquakes and friction laws. *Nature*, 391: 37–42
- Sieh K, Natawidjaja D H, Meltzner A J, Shen C C, Cheng H, Li K S, Suwargadi B W, Galetzka J, Philibosian B, Edwards R L. 2008. Earthquake supercycles inferred from sea-level changes recorded in the corals of West Sumatra. *Science*, 322: 1674–1678
- Sufri O, Koper K D, Lay T. 2012. Along-dip seismic radiation segmentation during the 2007  $M_w$  8.0 Pisco, Peru earthquake. *Geophys Res Lett*, 39: L08311
- Tinti E, Spudich P, Cocco M. 2005. Earthquake fracture energy inferred from kinematic rupture models on extended faults. *J Geophys Res*, 110: B12303
- Uchide T, Yao H, Shearer P M. 2013. Spatio-temporal distribution of fault slip and high-frequency radiation of the 2010 El Mayor-Cucapah, Mexico earthquake. *J Geophys Res-Solid Earth*, 118: 1546–1555
- Unsworth M J, Jones A G, Wei W, Marquis G, Gokarn S G, Spratt J E, Bedrosian P, Booker J, Leshou C, Clarke G, Shenghui L, Chanhong L, Ming D, Sheng J, Solon K, Handong T, Ledo J, Roberts B, Roberts B. 2005. Crustal rheology of the Himalaya and Southern Tibet inferred from magnetotelluric data. *Nature*, 438: 78–81
- Wang D, Mori J. 2011. Frequency-dependent energy radiation and fault coupling for the 2010  $M_w$  8.8 Maule, Chile, and 2011  $M_w$  9.0 Tohoku, Japan, earthquakes. *Geophys Res Lett*, 38: L22308
- Wang K, Fialko Y. 2015. Slip model of the 2015  $M_w$  7.8 Gorkha (Nepal) earthquake from inversions of ALOS-2 and GPS data. *Geophys Res Lett*, 42: 7452–7458
- Weng H, Huang J, Yang H. 2015. Barrier-induced supershear ruptures on a slip-weakening fault. *Geophys Res Lett*, 42: 4824–4832
- Weng H, Yang H, Zhang Z, Chen X. 2016. Earthquake rupture extents and coseismic slips promoted by damaged fault zones. *J Geophys Res-Solid Earth*, 121: 4446–4457
- Yagi Y, Okuwaki R. 2015. Integrated seismic source model of the 2015 Gorkha, Nepal, earthquake. *Geophys Res Lett*, 42: 6229–6235
- Yang H, Liu Y, Lin J. 2012a. Effects of subducted seamounts on megathrust earthquake nucleation and rupture propagation. *Geophys Res Lett*, 39: L24302
- Yang H, Liu Y, McGuire J J. 2012b. Modeling rupture segmentations on the Cascadia megathrust. In AGU Fall Meeting Abstracts. 2503
- Yang H, Liu Y, Lin J. 2013. Geometrical effects of a subducted seamount on stopping megathrust ruptures. *Geophys Res Lett*, 40: 2011–2016
- Yang H, Weng H. 2016. Frictional properties and fracture energy constrained from frequency-dependent coseismic radiations of great earthquakes, AGU Fall Meeting, Abstract S12A-06
- Yao H, Gerstoft P, Shearer P M, Mecklenbräuker C. 2011. Compressive sensing of the Tohoku-Oki  $M_w$  9.0 earthquake: Frequency-dependent rupture modes. *Geophys Res Lett*, 38: L20310
- Yao H, Shearer P M, Gerstoft P. 2013. Compressive sensing of frequency-dependent seismic radiation from subduction zone megathrust ruptures. *Proc Natl Acad Sci USA*, 110: 4512–4517
- Ye L, Lay T, Kanamori H, Rivera L. 2016. Rupture characteristics of major and great ( $M_w \geq 7.0$ ) megathrust earthquakes from 1990 to 2015: 2. Depth dependence. *J Geophys Res-Solid Earth*, 121: 845–863
- Yin A, Harrison T M. 2000. Geologic evolution of the Himalayan-Tibetan orogen. *Annu Rev Earth Planet Sci*, 28: 211–280
- Yin J, Yao H. 2016. Rupture and frequency-dependent seismic radiation of the 2012  $M_w$  8.6 Sumatra strike-slip earthquake. *Geophys J Int*, 205: 1682–1693
- Yin J, Yang H, Yao H, Weng H. 2016. Coseismic radiation and stress drop during the 2015  $M_w$  8.3 Illapel, Chile megathrust earthquake. *Geophys Res Lett*, 43: 1520–1528
- Yue H, Simons M, Duputel Z, Jiang J, Fielding E, Liang C, Owen S, Moore A, Riel B, Ampuero J P, Samsonov S V. 2016. Depth varying rupture properties during the 2015  $M_w$  7.8 Gorkha (Nepal) earthquake. *Tectonophysics*
- Zhang H, van der Lee S, Ge Z. 2016. Multiarray rupture imaging of the devastating 2015 Gorkha, Nepal, earthquake sequence. *Geophys Res Lett*, 43: 584–591
- Zhang P Z, Shen Z, Wang M, Gan W, Bürgmann R, Molnar P, Wang Q, Niu Z, Sun J, Wu J, Hanrong S, Xinzhaoy Y. 2004. Continuous deformation of the Tibetan Plateau from global positioning system data. *Geology*, 32: 809–812